Catal Lett (2009) 127:63–69
DOI 10.1007/s10562-007-9353-9

A Chemical Potential Diagram and an In-situ X-ray Diffraction Analysis of a V–Mg–O Catalyst Used in the Oxidative Dehydrogenation of *n*-Butane

Norihito Kijima · Makoto Toba · Yuji Yoshimura

Received: 6 January 2007 / Accepted: 13 November 2007 / Published online: 19 September 2008

Abstract A chemical potential diagram of the V–Mg–O system was constructed for comparison in an in-situ experiment. A V–Mg–O catalyst used in the oxidative dehydrogenation of *n*-butane was prepared by the impregnation method and was characterized by in-situ X-ray diffraction (XRD). $Mg_3V_2O_8$ and MgO were detected on the in-situ XRD pattern under the oxygen pretreatment at 600 °C, and the in-situ XRD data under working conditions showed that $Mg_3V_2O_8$ is reduced to MgV_2O_4, having a cubic spinel structure with a lattice constant of a = 8.427 Å. The observed reduction of V^{5+} in $Mg_3V_2O_8$ to V^{3+} in MgV_2O_4 under the working conditions could be well understood through a chemical potential diagram.

Keywords V–Mg–O Catalyst · Oxidative dehydrogenation of *n*-butane · Chemical potential diagram · In-situ X-ray diffraction

1 Introduction

In industrial use of a catalyst, its durability is more important in many cases rather than its activity and selectivity. Although the stability of a catalyst under working conditions is most important, there are few trials which are going to predict the stability of a catalyst before using it. Chemical potential diagrams are expected to provide us with useful information for catalyst development, such as appropriate working, reforming, and preparation conditions.

Industrial catalysts usually contain many metal elements. In a system composed of many elements, its thermodynamic calculation becomes more complicated than that for binary systems. An attempt has been made to construct a stability diagram in metal–metal–nonmetal systems, and a plot of mole fraction versus oxygen potential can clearly provide phase relations among alloys and oxide solid solutions [1]. However, this diagram is not appropriate for presenting many stoichiometric compounds because they are presented as lines, making it difficult to distinguish them from equilibrium tie lines. To visualize complicated equilibria among these stoichiometric compounds, it would be useful to construct a complete chemical potential diagram for metal–metal–nonmetal systems which can present each compound as a polygon, not as a line.

To demonstrate the application of chemical potential diagrams in developing catalysts, we preliminarily constructed a chemical potential diagram of the V–Mg–O system [2]. The V–Mg–O system is a good example because it is not a simple binary metal–nonmetal system but a complicated ternary metal–metal–nonmetal system.

In the last decades, many researchers have been working on highly active and selective catalysts for the oxidative dehydrogenation of alkanes. V–Mg–O catalysts are among the most selective and active catalysts for the oxidative dehydrogenation of *n*-butane to butene and butadiene as well as of propane to propene [3–18]. The active phase for the V–Mg–O catalysts has been the subject of controversy. Most proposals in the literature have favored a bulk V–Mg–O phase, e.g., $Mg_2V_2O_7$ and $Mg_3V_2O_8$ [10–14]. However, later research works have suggested that monomeric and polymeric vanadia species supported on MgO are the source of catalytic activity [15–18].

N. Kijima (✉) · M. Toba · Y. Yoshimura
National Institute of Advanced Industrial Science and Technology (AIST), Tsukuba Central 5, 1-1-1 Higashi, Tsukuba, Ibaraki 305-8565, Japan
e-mail: n-kijima@aist.go.jp

In order to discuss the application of chemical potential diagrams in developing catalysts, the chemical potential diagram should be compared with the result of an in-situ experiment. In this paper, the chemical potential diagram of the V–Mg–O system was constructed in considerable detail, and the V–Mg–O catalyst was characterized by in-situ X-ray diffraction (XRD). From the comparison of the chemical potential diagram and the in-situ XRD analysis, we ascertained that the chemical potential diagram can predict the reduction process of the catalyst under the working conditions.

2 Experimental

2.1 Catalyst Preparation

A V–Mg–O catalyst was prepared by the impregnation method. Reagent-grade $Mg(OH)_2$ and NH_4VO_3 were purchased from Soekawa Chemical Co. Ltd., and NH_3 solution was obtained from Wako Pure Chemical Ind. Co. Ltd. NH_4VO_3 was dissolved in 1% NH_3 solution and was then heated to 80 °C. Subsequently, $Mg(OH)_2$ was added to the hot solution with continuous stirring. This suspension was evaporated and dried overnight at 120 °C. The resulting solid was crushed and calcined under air at 800 °C for 6 h. The atomic ratio of Mg and V elements was fixed at Mg:V = 6:1. The nominal V content in the catalyst was 15.3 wt.%, which was calculated by assuming that all metal elements in the product were oxidized completely. In this paper, the catalyst is referred to as 15 V/VMgO.

2.2 Measurements

2.2.1 Catalytic Performance

Catalytic tests were carried out at atmospheric pressure in a conventional fixed-bed continuous-flow reactor. The high-purity gases, n-C_4H_{10} (99.9%), O_2 (99.9%), and N_2 (99.9%), were used in the experiments. The products of the reaction were analyzed by an on-line gas chromatograph equipped with a thermal conductivity detector and a flame ionization detector. The conversion and selectivity were calculated based on the reacted n-C_4H_{10}. N_2 in the feed was used as an internal standard for calculations of conversion and selectivity. Powder catalysts were pressed binder-free, crushed, and sieved to a particle size of 75–150 μm. These particles were diluted with inert quartz particles and were mounted in the middle of a quartz tube reactor. To minimize the extent of gas phase reactions, the volume in the reactor, except for catalyst, was packed with the quartz particles. The catalytic zone was heated to 600 °C in a flow of O_2 and kept at 600 °C for 1 h before the catalytic test. The reactant mixture (n-$C_4H_{10}/O_2/N_2$) was then introduced into the reactor.

2.2.2 In-situ X-ray Diffraction

In-situ powder XRD data were taken with the Bragg–Brentano type powder diffractometer with a vertical θ-θ geometry. To permit studies of catalysts under in-situ conditions, its goniometer was equipped with a high-temperature chamber. The well-crushed catalyst was packed in an alumina holder as thick as 5 mm, and the temperature was measured by a chromel–alumel thermocouple located on the sample holder. The same gases used for catalytic tests were used for the in-situ XRD experiments. The flow rate of the gases was controlled by a thermal mass flow controller. The temperature was maintained all time at 600 °C without cooling or reheating. A Cu Kα radiation ($\lambda = 1.54018$ Å), which was generated by a rotating anode at 40 kV and 300 mA, was used. The intensity data were collected between $2\theta = 10°$–$60°$ with a step interval of 0.04°. The scanning speed was 1.0°/min, and diffraction patterns did not change during measurements. Mass fractions of compounds contained in the sample were calculated from the XRD data with the computer program RIETAN-2000 [19, 20]. The theoretical background of this calculation is presented in the literature [21, 22].

2.3 Thermodynamic Data and Calculation

Table 1 lists the thermodynamic data used in the present study. These data have been registered in the thermodynamic database MALT2 (Materials-oriented Little Thermodynamic database) [23]. The thermodynamic data in MALT2 were generally taken from major data books [24–26], and because of the absence of experimental data, some data of oxides were estimated empirically by Yokokawa et al. [23, 27]. Chemical potential diagrams were constructed using the computer program CHD [28–30]. A $\log(a_V/a_{Mg})$ vs. $P(O_2)_{cal}$ plot was adopted for the present investigation, where a_V is the activity for V element, a_{Mg} is the activity for Mg element, and $P(O_2)_{cal}$ is the equilibrium oxygen pressure estimated by the thermodynamic calculation.

3 Results and Discussion

3.1 Catalytic Performance

Table 2 lists the catalytic performances of the 15 V/VMgO catalyst at 600 °C. The catalyst was generally active

Table 1 Thermodynamic parameters used in the present study[a]

Element/State[b]	Compound	$\Delta_f H°$ (kJ/mol)	$\Delta_f G°$ (kJ/mol)	$S°$ (J/(Kmol))	a	b	c	d	e	T(°C)	$\Delta_{tr} H°$ (kJ/mol)
O_2	g	0	0	205.029	34.35	1.92	−18.45		4.06	25–2226.85	
Mg	c	0	0	32.68	28.51	−6.799	−2.439	13.05		25–648.85(mp)[c]	8.9500
	l				22.09	10.88				648.85–1105.73(bp)[c]	127.4580
V	c	0	0	28.91	25.806	0.909	−1.676	3.245		25–1946.85(mp)[c]	23.0
MgO	c	−601.7	−569.45	26.94	49.45	3.31	−16.9		1.51	25–2831.85(mp)[c]	77.82
VO	c	−431.74	−402.547	33.51	52.92	13.113	−16.365			25–1789.85(mp)[c]	50.0
V_2O_3	c	−1218.7	−1138.98	94.64	144.31	−18.663	−34.45	10.892		25–1956.85(mp)[c]	140.0
V_3O_5	c	−1938.79	−1805.95	153.75	216.66	−9.133	−48.82	10.892		25–2226.85	
V_4O_7	c	−2651.6	−2466.8	213.3	289.01	0.397	−63.19	10.892		25–2226.85	
V_5O_9	c	−3361.6	−3124.8	272.9	361.36	9.927	−77.56	10.892		25–2226.85	
V_6O_{11}	c	−4071.0	−3782.2	332.5	433.71	19.457	−91.93	10.892		25–2226.85	
V_7O_{13}	c	−4780.0	−4439.2	392.0	506.06	28.987	−106.3	10.892		25–2226.85	
V_8O_{15}	c	−5489.1	−5096.1	450.73	578.41	38.517	−120.67	10.892		25–1226.85	
V_9O_{17}	c	−6198.3	−5753.0	509.36	650.76	48.047	−135.04	10.892		25–1226.85	
$V_{10}O_{19}$	c	−6907.3	−6409.8	568.1	704.17	88.53	−122.29			25–1226.85	
V_2O_4	c1	−1424.2	−1312.5	93.18	364.962	−1906.1		3548.9		25–65.55(tp)[c]	9.15
	c2				144.694	19.061	−28.737			65.55−1544.85(mp)[c]	112.0
V_6O_{13}	c	−4383.9	−4045.1	369.9	454.59	59.63	−90.87			25–726.85	
V_3O_7	c	−2281.0	−2098.0	190.6	237.32	31.85	−50.15			25–726.85	
V_2O_5	c	−1550.7	−1419.6	130.8	190.878	−92.779	−39.034	95.232		25–680.85(mp)[c]	64.0
	l				190.8					680.85–1689.85(dp)[c]	
$MgVO_3$	c	−1349.1	−1261.0	73.7	121.89	12.57	−30.48		1.51	25–1019.85(dp)[c]	
MgV_2O_4	c	−1840.5	−1728.6	125.24	174.26	17.76	−34.63		1.51	25–1226.85	
MgV_2O_5	c	−2070.1	−1926.8	122.44	194.3	21.83	−44.4		1.51	25–949.85(dp)[c]	
MgV_2O_6	c1	−2201.58	−2039.41	160.7	214.34	25.9	−53.47		1.51	25–566.85(tp)*	
	c2				214.34	25.9	−53.47		1.51	566.85–759.85(dp)*	
Mg_2VO_4	c	−1967.0	−1848.0	105.13	171.325	15.88	−47.375		3.02	25–1226.85	
$Mg_2V_2O_7$	c1	−2835.92	−2645.29	200.4	263.79	29.21	−70.37		3.02	25–708.85(tp)[c]	19.63
	c2				263.79	29.21	−70.37		3.02	708.85–906.85(tp)[c]	10.0
	c3				263.79	29.21	−70.37		3.02	906.85–949.85(dp)[c]	
$Mg_3V_2O_8$	c	−3445.8	−3227.8	244.9	313.24	32.52	−87.27		4.53	25–1164.85	

[a] Definitions: $\Delta_f H°$, standard enthalpy of formation; $\Delta_f G°$, standard Gibbs' free energy of formation; $S°$, standard entropy; $\Delta_{tr} H°$, enthalpy of transformation. Heat capacity coefficients, a–e, given by the following equation: $C_p = a + (b \times 10^{-3})T + (c \times 10^5)T^{-2} + (d \times 10^6)T^2 + (e \times 10^8)T^{-3}$

[b] g: gas; l: liquid; c, c1, c2, c3: solids

[c] mp: melting point; bp: boiling point; tp: transformation point; dp: decomposition point

Table 2 Catalytic performances of the 5 V/MgVO catalyst in the oxidative dehydrogenation of *n*-butane[a]

Flow rate (cm^3/min)	Conversion (%)		Selectivity (%)						
n-$C_4H_{10}/O_2/N_2$	n-C_4H_{10}	O_2	C_1–C_3	1-C_4H_8	*trans*−2-C_4H_8	*cis*-2-C_4H_8	C_4H_6	CO	CO_2
4/8/88	24.1	34.5	6.1	12.3	4.6	4.8	21.1	19.8	31.1
2/4/94	28.2	35.8	5.0	11.9	4.1	4.7	22.7	22.8	28.8
2/1/97	30.4	95.1	6.0	18.2	6.8	7.9	37.7	11.2	12.2

[a] Reaction conditions: $T = 600$ °C, n-$C_4H_{10}/O_2/N_2 = 2/1/97$ cm^3/min, catalyst: 0.3 g

beginning at about 500 °C. The dominant products were dehydrogenation products (1-C_4H_8, 2-*trans*-C_4H_8, 2-*cis*-CH_8, and C_4H_6) and combustion products (CO and CO_2). Small amounts of CH_4, C_2H_4, and C_3H_6 were also observed. The carbon balances were nearly 100%. The conversion of both n-C_4H_{10} and O_2 remained almost constant within 6 h periods. The tendency of selectivities to dehydrogenation and combustion products is consistent with the earlier works.

3.2 Chemical Potential Diagrams of V–Mg–O System

Figure 1 depicts the chemical potential diagram of the V–Mg–O system at 600 °C. In the ternary V–Mg–O system, seven double oxides—$MgVO_3$ [31], MgV_2O_5 [32], MgV_2O_4 [33], Mg_2VO_4 [34], MgV_2O_6 [35], $Mg_2V_2O_7$ [36], $Mg_3V_2O_8$ [37]—were considered. Both MgV_2O_4 and Mg_2VO_4 have a spinel structure, and their solid solution, $Mg_{2-x}V_{1+x}O_4$, is known [38]. Same other double oxides are reported in the V–Mg–O system [39, 40]. In this study, those double oxides and $Mg_{2-x}V_{1+x}O_4$ were neglected. The following features can be considered from Fig. 1.

(1) On the left axis in Fig. 1, Mg and V areas are divided by the horizon line at $\log(a_V/a_{Mg}) = 0$ because they make no alloys. In the Mg–V system, no intermetallic compounds have been registered in the inorganic crystal structure database (ICSD) [40].

(2) Phase relations associated with the binary V–O and Mg–O systems are plotted in the upper and lower axes, respectively. For example, lines A and B in Fig. 1 correspond to point A in Fig. 2 and point B in Fig. 3, respectively. Although MgO and MgO_2 are known in the Mg–O system [30], MgO was alone considered in this study because of the lack of thermodynamic data. In Fig. 3, some vanadium oxides listed in Table 1 were omitted because of congestion.

(3) Equilibrium among the three phases appears as a point in the diagram. Fig. 4 exemplifies the temperature dependency of the equilibrium oxygen pressure of the reaction: $2MgO + 2Mg_3V_2O_8 = 4Mg_2VO_4 + O_2$. The decomposition oxygen pressure of $Mg_3V_2O_8$ is $P(O_2)_{cal} = 4.59 \times 10^{-5}$ Pa at 600 °C (point C in Fig. 4) that corresponds to point C in Fig. 1.

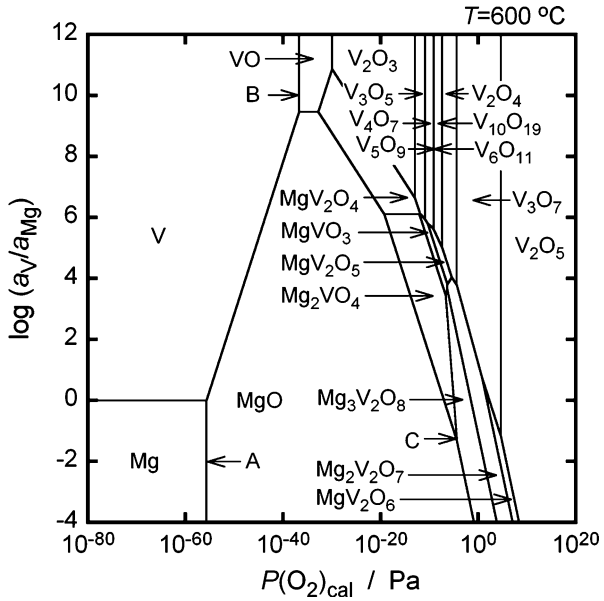

Fig. 1 Chemical potential diagram of the V–Mg–O system at 600 °C

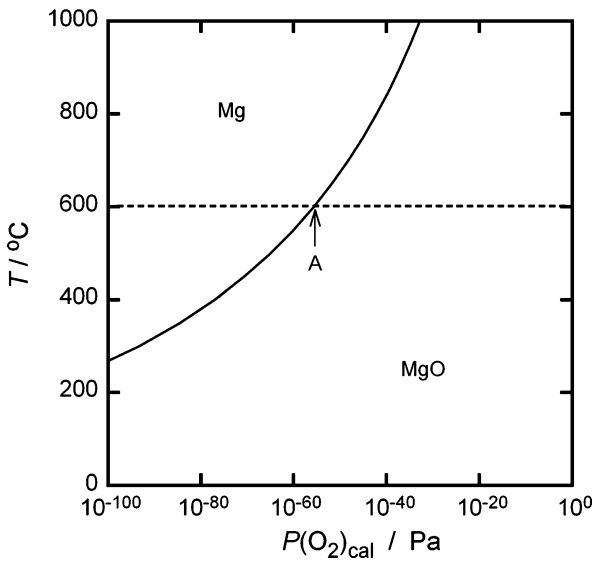

Fig. 2 $P(O_2)_{cal}$-T diagram of the Mg–O system

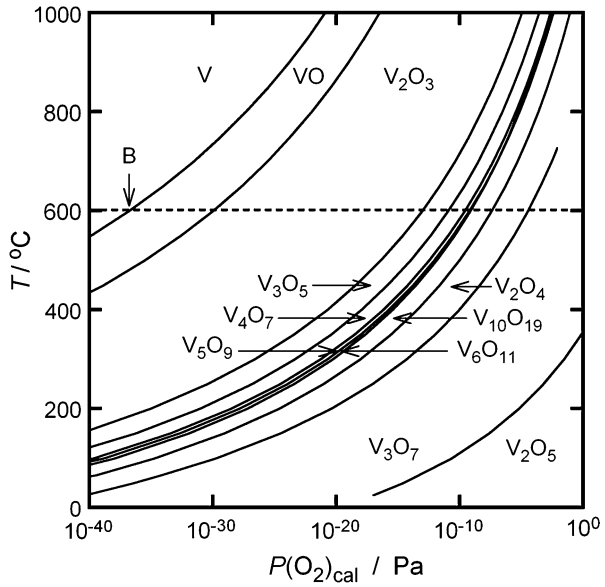

Fig. 3 $P(O_2)_{cal}$-T diagram of the V–O system

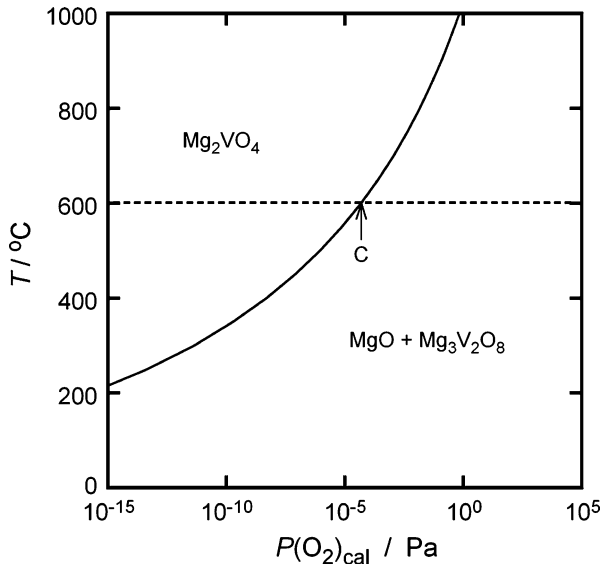

Fig. 4 Temperature dependency of the equilibrium oxygen pressure for the reaction: $2MgO + 2Mg_3V_2O_8 = 4Mg_2VO_4 + O_2$

(4) When a double oxide changes to a double oxide with other valence state of V, their respective areas appear in series along the $P(O_2)_{cal}$ axis. For example, $Mg_3V_2^{+5}O_8$ is reduced to $Mg_2V^{+4}O_4$ and then changes to $MgV_2^{+3}O_4$ when $P(O_2)_{cal}$ decreased.

3.3 In-situ X-ray Diffraction

Figure 5 shows the in-situ XRD patterns of the 15 V/VMgO catalyst under working conditions at 600° C. Table 3 summarizes the V content in the 15 V/VMgO catalyst

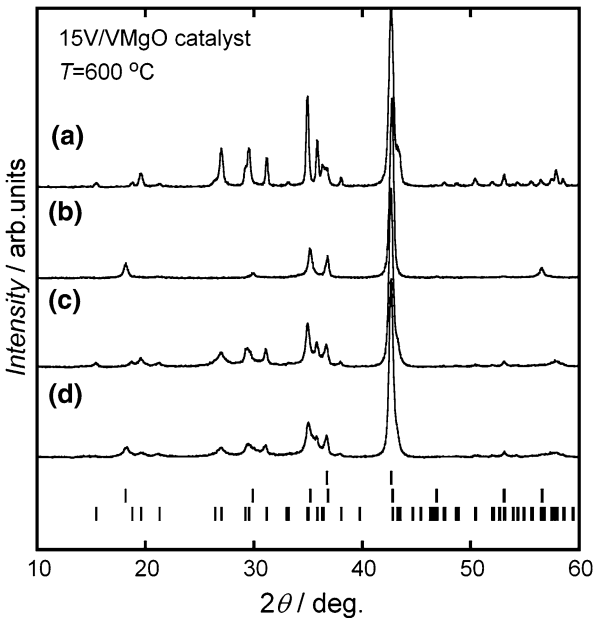

Fig. 5 In-situ XRD patterns of the 15 V/VMgO catalyst under several conditions at 600 °C. The short vertical lines below the profiles indicate the peak positions of all the possible Bragg reflections of MgO (upper), MgV_2O_4 (middle), and $Mg_3V_2O_8$ (lower). Data were collected after 2 h in a flow of (a) $O_2 = 200$ cm^3/min, (b) n-$C_4H_{10}/O_2/N_2 = 2/0.2/197.8$ cm^3/min, (c) $O_2 = 200$ cm^3/min (re-oxidation), and (d) n-$C_4H_{10}/O_2/N_2 = 2/0.2/197.8$ cm^3/min after the re-oxidation

Table 3 V content in the 15 V/VMgO catalyst calculated from the in-situ XRD data under working conditions

V content (wt.%)	Mass fraction (wt.%)			Flow rate of gases (cm^3/min)			Temperature (°C)	Time course (h)
	MgO	Mg_2O_8	MgV_2O_4	n-C_4H_{10}	O_2	N_2		
11.8	68.87	35.13	–	0	200	0	600	2
7.7	85.62	–	14.38	2	0.2	197.8	600	4
8.3	75.33	24.67	–	0	200	0	600	6
7.8	78.89	17.86	3.25	2	0.2	197.8	600	8

calculated from the in-situ XRD data. Mass fractions of compounds contained in the sample were analyzed by Rietveld refinment [19–22], and the V contents in the catalyst were estimated from mass fractions of the observed compounds.

Figure 5a displays that $Mg_3V_2O_8$ and MgO were detected during the oxygen pretreatment. The lattice constants were a = 6.093 Å, b = 11.427 Å, and c = 8.318 Å for $Mg_3V_2O_8$, and a = 4.222 Å for MgO. Figure 5b demonstrates that MgV_2O_4 was newly detected and that $Mg_3V_2O_8$ had disappeared after being exposed to the reaction gas (n-$C_4H_{10}/O_2/N_2$ = 2/0.2/197.8 cm^3/min) for 2 h. The lattice constant of MgV_2O_4 was a = 8.427 Å.

Burrows et al. carried out the in-situ XRD and in-situ X-ray absorption fine structure (XAFS) studies of a Mg–V–O catalyst under conditions of the oxidative dehydrogenation of propane [17]. When the catalyst was exposed to the working atmosphere (1% C_3H_8/0.1% O_2/98.9% He) at 500 °C, the in-situ XRD pattern showed that $Mg_3V_2O_8$ was transformed to a cubic spinel type structure with a lattice constant of 8.42 Å, and the in-situ XAFS spectrum indicated a change in valence state of V from 5+ to 3+ [17].

Our in-situ XRD data showed that the lattice constant of the spinel phase was a = 8.427 Å, which is in good agreement with that reported by Burrows et al. [17]. They are closer to a = 8.42 Å for MgV_2O_4 [32] than a = 8.391 Å for Mg_2VO_4 [34]. We, therefore, concluded that $Mg_3V_2O_8$ having V^{5+} is reduced to MgV_2O_4 having V^{3+} under the working conditions. Since the solid solution of those spinel compounds is known [38], V^{3+} and V^{4+} would coexist in the $Mg_{2-x}V_{1+x}O_4$ phase if the catalyst is used at higher $P(O_2)$ regions.

Figure 5c shows that $Mg_3V_2O_8$ was again produced but that MgV_2O_4 could not be detected when the catalyst was reformed under oxygen gas. As can be seen in Fig. 5d, MgV_2O_4 was again generated, but $Mg_3V_2O_8$ remained partly when this catalyst was exposed to the reaction gas after the re-oxidation. In our in-situ XRD data, the phase transformation of $Mg_3V_2O_8$ to MgV_2O_4 was irreversible. However, Burrows et al. reported that the phase transformation was reversible at typical reaction temperatures [17]. The reactivity of the V–Mg–O catalyst would depend on applied preparation methods.

As Table 3 lists, the V content in the 15 V/VMgO catalyst calculated from the XRD data differed from its nominal composition. Furthermore, the V content in the catalyst exposed to the reaction gas was smaller than that for the unused catalyst. These facts show that undetectable vanadia species other than the bulk $Mg_3V_2O_8$ or MgV_2O_4 phases also exist on the catalyst surface, and the amount of such species is variable depending on each reaction condition.

3.4 Comparison of Chemical Potential Diagram and In-situ X-ray Diffraction

The in-situ XRD data showed that $Mg_3V_2O_8$ and MgO are stable under oxygen pretreatment where the partial pressure of oxygen in the gas phase, $P(O_2)_{gas}$, is 1.01×10^5 Pa (100% O_2). This finding is consistent with the chemical potential diagram. Most as-prepared V–Mg–O catalysts reported in the literature contain the $Mg_3V_2O_8$ phase.

The observed reduction process of the bulk V–Mg–O phase under the working conditions can be also well understood by the chemical potential diagram. Figure 1 shows that $Mg_3V_2O_8$ is reduced to MgV_2O_4 at lower $P(O_2)_{cal}$ regions. This reduction process is consistent with our in-situ XRD data.

The in-situ XRD data demonstrated that MgV_2O_4 is generated under the conditions of the typical oxidative dehydrogenation of n-butane. From the in-situ condition (n-$C_4H_{10}/O_2/N_2$ = 2/0.2/197.8 cm^3/min), $P(O_2)_{gas}$ can be estimated to be 1.01×10^3 Pa (1% O_2). Figure 1, however, shows that Mg_2VO_4 is stable at $P(O_2)_{cal} = 8.91 \times 10^{-13}$ -1.74×10^{-33} Pa. These findings show that the surface of the catalyst is exposed to a rather high reduction state compared with the gas phase because of reducing gases, e.g., CO and H_2, being present near the catalyst surface.

Finally, we should mention that undetectable vanadia species other than the bulk V–Mg–O phase also exist on the catalyst surface because the V content in the 15 V/VMgO catalyst calculated from the XRD data differed from its nominal composition. No information concerning such species can be obtained neither by in-situ XRD analysis nor from the chemical potential diagram. However, the stability of undetectable vanadia species is not independent of that of the bulk phase. The durability of a catalyst would be speculated from the stability of bulk.

4 Conclusion

In order to discuss the application of chemical potential diagrams in developing catalysts, we compared the chemical potential diagram with the result of the in-situ XRD analysis. In this study, the observed reduction of V^{5+} in $Mg_3V_2O_8$ to V^{3+} in MgV_2O_4 under the working conditions could be well understood through a chemical potential diagram. From this comparison, it was also ascertained that the surface of the catalyst is exposed to a rather high reduction state compared with the gas phase because of reducing gases, e.g., CO and H_2, being present near the catalyst surface.

The stability of the bulk V–Mg–O phase can be considered well by the chemical potential diagram. On the other hand, the undetectable vanadia species on the surface

cannot be identified from the chemical potential point of view. The prediction of the calculated chemical potential would be particularly relevant for catalytic systems working either under lean or rich conditions, such as a circulating bed reactor. However, the calculations are non operative when only a small part of surface metal ions are cycling during the redox process. By choosing the application range, chemical potential diagrams provide us with useful information for catalyst development.

Acknowledgment We would like to thank Dr. H. Yokokawa at AIST for his valuable discussion.

References

1. Pelton AD, Thompson WT (1979) Prog Solid State Chem 10:119–155
2. Yoshimura Y (1998) Shokubai 40:608–616 [In Japanese]
3. Kung HH (1994) Adv Catal 40:1–38 and references therein
4. Mamedov EA, Cortés Corberán V (1995) Appl Catal A 127:1–40 and references therein
5. Cavani F, Trifirò F (1995) Catal Today 24:307–313 and references therein
6. Albonetti S, Cavani F, Trifirò F (1996) Catal Rev-Sci Eng 38:413–438 and references therein
7. Kung HH, Kung MC (1997) Appl Catal A 157:105–116 and references therein
8. Blasco T, López Nieto JM (1997) Appl Catal A 157:117–142 and references therein
9. Madeira LM, Portela MF (2002) Catal Rev-Sci Eng 44:247–286 and references therein
10. Chaar MA, Patel D, Kung MC, Kung HH (1987) J Catal 105:483–498
11. Siew Hew Sam D, Soenen V, Volta JC (1990) J Catal 123:417–435
12. Gao X, Ruiz P, Xin Q, Guo X, Delmon B (1994) Catal Lett 23:321–337
13. Gao X, Ruiz P, Xin Q, Guo X, Delmon B (1994) J Catal 148:56–67
14. Soenen V, Herrmann JM, Volta JC (1996) J Catal 159:410–417
15. Pantazidis A, Aurouxv, Herrmann J-M, Mirodatos C (1996) Catal Today 177:81–88
16. Pantazidis A, Burrows A, Kiely CJ, Mirodatos C (1998) J Catal 177:325–334
17. Burrows A, Kiely CJ, Perregaard J, Højlund-Nielsen PE, Vorbeck G, Calvino JJ, López-Cartes C (1999) Catal Lett 57:121–128
18. Pak C, Bell AT, Tilley TD (2002) J Catal 206:49–59
19. Izumi F, Ikeda T (2000) Mater Sci Forum 321–324:198–203
20. Izumi F (1995) In: Young RA (ed) The Rietveld Method (Chapter 13). Oxford University Press, Oxford, p 12
21. Bish DL, Howard SA (1988) J Appl Crystallogr 21:86–91
22. Hill RJ (1995) In: Young RA (ed) The Rietveld Method (Chapter 5). Oxford University Press, Oxford and references therein
23. Thermodynamic Database MALT2 (1992) The Japan society of calorimetry and thermal analysis. Kagaku Gijutsu-sha
24. Wagman DD, Evans WH, Parker VB, Schumm RH, Halow I, Bailey SM, Churney KL, Nuttall RL (1982) The NBS tables of chemical thermodynamic properties. J Phys Chem Ref. Data 11 Supplement No. 2
25. Chase MW Jr, Davies CA, Downey JR Jr, Frurip DJ, McDonald RA, Syverud AN (1985) JANAF Thermodynamical Tables, 3rd edn. J Phys Chem Ref. Data 14 Supplement No. 1
26. Glushkov VP, Gurvich LV, Bergman GA, Veitz IV, Medvedev VA, Khachkuruzov GA, Yungman VA, Thermodynamic data for individual substances. High Temperature Institute, State Institute of Applied Chemistry, National Academy of Sciences of the USSR, Moscow, 1978, 1979, 1981, 1982
27. Yokokawa H, Sakai N, Kawada T, Dokiya M (1991) J Solid State Chem 94:106–120
28. Yokokawa H, Kawada T, Dokiya M (1989) J Am Ceram Soc 72:2104–2110
29. Yokokawa H, Sakai N, Kawada T, Dokiya M (1990) J Am Ceram Soc 73:649–658
30. Yokokawa H (1999) J Phase Equilibria 20:258–287
31. Bouloux J-C, Milosevic I, Galy J (1976) J Solid State Chem 16:393–398 [In French]
32. Millet P, Satto C, Sciau P, Galy J (1998) J Solid State Chem 136:56–62
33. Reuter B, Aust R, Colsmann G, Neuwald C (1983) Anorg Z Allg Chem 500:188–198
34. Rüdorff W, Reuter B (1947) Anorg Z Chem 253:194–208
35. Ng HN, Calvo C (1972) Canad J Chem 50:3619–3624
36. Gopal R, Calvo C (1974) Acta Crystallogr Sect B 30:2491–2493
37. Krishnamachari N, Calvo C (1971) Canad J Chem 49:1629–1637
38. Oshima H (1983) J Am Ceram Soc 66:482–485
39. Clark GM, Morley R (1976) J Solid State Chem 16:429–435 and references therein
40. Inorganic Crystal Structure Database (ICSD), Version: 2007-01, the National Institute of Standards and Technology, Fachinformationszentrum Karlsruhe, 2007